**NJC**

# Molten aluminum doping porous silicon anodes enable high initial coulombic efficiency and stability

| | |
|---:|:---|
| Journal: | *New Journal of Chemistry* |
| Manuscript ID | NJ-COM-09-2024-003942.R1 |
| Article Type: | Communication |
| Date Submitted by the Author: | 26-Oct-2024 |
| Complete List of Authors: | Yan, Xiangshun; Shandong University of Science and Technology College of Mechanical and Electronic Engineering, College of Mechanical and Electronic Engineering<br>Chen, Yuan; Shandong University of Science and Technology College of Mechanical and Electronic Engineering<br>Wang, Yongshu; Shandong University of Science and Technology College of Mechanical and Electronic Engineering, College of Mechanical and Electronic Engineering<br>Wu, Fan; Shandong University of Science and Technology College of Mechanical and Electronic Engineering, College of Mechanical and Electronic Engineering<br>Wang, Wensheng; Shandong University of Science and Technology College of Mechanical and Electronic Engineering, College of Mechanical and Electronic Engineering<br>Zhang, Wei; Shandong University of Science and Technology College of Mechanical and Electronic Engineering, College of Mechanical and Electronic Engineering<br>Yang, Xin; Shandong University of Science and Technology, College of Energy Storage Technology<br>Bai, Zhongchao; Shandong University of Science and Technology College of Mechanical and Electronic Engineering<br>Dong, Chao; The University of Texas of the Permian Basin Department of Physical Sciences<br>Moore, Antonio; Fisk University, Department of Life and Physical Sciences<br>Zhang, Qiang; Shandong University of Science and Technology College of Mechanical and Electronic Engineering |
| | |

**SCHOLARONE**™
Manuscripts

# Molten aluminum doping porous silicon anodes enable high initial coulombic efficiency and stability

Xiangshun Yan,[a,b] Yuan Chen,*[a] Yongshu Wang,[a,b] Fan Wu,[a,b] Wensheng Wang,[a,b] Wei Zhang,[a,b] Xin Yang,[b] Zhongchao Bai,[a] Chao Dong,[c] Antonio Moore[d] and Qiang Zhang[a]

**The aluminum-doped porous silicon was produced by a molten salt reaction. It showed accelerated lithium-ion diffusion kinetics and excellent structural stability. The pSi-Al significantly reduced the charge/ion transport resistance and first lithium capture by Al doping. It also affected the generation of SEI in the cycle and promoted the formation of LiF. The achieved ICE was 90.57 % and initial reversible capacity was 2860 mAh g$^{-1}$. Moreover, the reversible capacity was 1765 mAh g$^{-1}$ after 100 cycles at 1 A g$^{-1}$, which demonstrated good electrochemical performance.**

## Introduction

The silicon-based anodes have drawn much attention in high energy density lithium Ion Batteries (LIBs).[1-3] However, the severe volume expansion, low conductivity, low Li$^+$ diffusion coefficients, and excessive depletion of the Li source,[4-7] leading to poor stability and lower ICE (65~85 %).[8, 9] Therefore, researchers have put much effort to enhance the stability and ICE of silicon anodes.

To strengthen the stability, the strategies include reducing particle size and creating nanostructures are developed, such as nanoparticles,[10] nanowires,[11] thin films,[12] and porous structures. Alternatively, surface coatings, compositing with metal or carbon,[13, 14] pre-lithium[15] are usually employed. Additionally, nanoization and porosity can significantly reduce the material's volume expansion. For example, the ant's nest porous silicon obtained the reversible capacity of 1,271 mAh g$^{-1}$ at 2 A g$^{-1}$.[16] The three-dimensional interconnected nanostructure could effectively prevent

particle pulverization and accommodate volume expansion during cycling.

Moreover, the ICE of silicon anodes are usually below 85 %. The heteroatom doping was demonstrated to be an efficient route to improve the ICE, such as phosphorus,[18] boron,[19] or metals.[20-22] For instance, Ma et al[23] have reported a molten salt alloying/dealloying method to prepare the 3D nanoporous silicon material (np-Si), which showed the ICE of 77.5 % and the capacity retention was 83 % after 1000 cycles. Xu et al[24] developed the Sn-doped Si (Sn-pSi), which showed the ICE of 84.3 %, and the capacity of 1165 mAh g$^{-1}$ after 400 cycles at 1 A g$^{-1}$. The Si@SiOx/Ag reported by Zhang et al showed the ICE of 89.7 %, and initial discharge capacity of 2919 mAh g$^{-1}$ at 500 mA g$^{-1}$.[25] Doping could not only increase the conductivity, but also regulate reaction kinetics such as Li alloying and SEI growth.[24] Therefore, developing new ways to precisely regulate the atomic structures of silicon anodes is expected to achieve higher electrochemical performance. As the radius of Al was close to Si, substitution could not cause obvious lattice deformation.

In this work, we proposed a molten salt assisted aluminum-doped and porous strategy to strengthen the conductivity and stability of silicon anode. The pSi-Al anode exhibited enhanced lithium storage performance in terms of excellent cycling stability and rate performance.

## Results and discussion

The synthesis steps of pSi-Al was illustrated in Fig. 1(a). The reaction was given in equation (1).

$$3Mg_2Si + 4AlCl_3 \rightarrow 6MgCl_2 + 4Al + 3Si \quad (1)$$
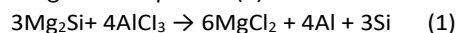
The initial product was confirmed by X-ray diffraction (XRD) after water washing. It consisted of Al, Si, and under-reacted Mg$_2$Si (Fig. S1). Transmission electron microscopy (TEM) was used to examine the microstructure of pSi-Al (take the 300 °C sample, named SA300). Fig. 1(b) and (c) displayed abundant porous structure, which agreed with the scanning electron microscopy (SEM) images (Fig. S2(a) and (b) ). The high-resolution TEM and selected area electron diffraction (SAED)

[a.] College of Mechanical and Electronic Engineering, Shandong University of Science and Technology, Qingdao 266590, China.

[b.] College of Energy Storage Technology, Shandong University of Science and Technology, Qingdao 266590, China.

[c.] Department of Chemistry and Physics, The University of Texas of the Permian Basin, 4901 E University Blvd Odessa TX 79762, USA.

[d] Department of Life and Physical Sciences, Fisk University, 1000 17th Ave N Nashville TN 37208, USA.

† Footnotes relating to the title and/or authors should appear here.

Supplementary Information available: [details of any supplementary information available should be included here]. See DOI: 10.1039/x0xx00000x

showed clear lattice stripes and diffraction rings (Fig. 1(d) and (e)). Lattice spacing measured at 0.188 nm (Fig. S2(c)). It was slightly smaller than the (220) crystal plane spacing of silicon. The distribution of lattice puncta of SA300 was obtained after the Fourier transform (Fig. 1(e) insert). The Energy Dispersive X-Ray (EDX) spectroscopy suggested the Si and Al distributed uniformly in the whole particle (Fig. (f~i)). It meant Al had been successfully introduced into the lattice of Si.
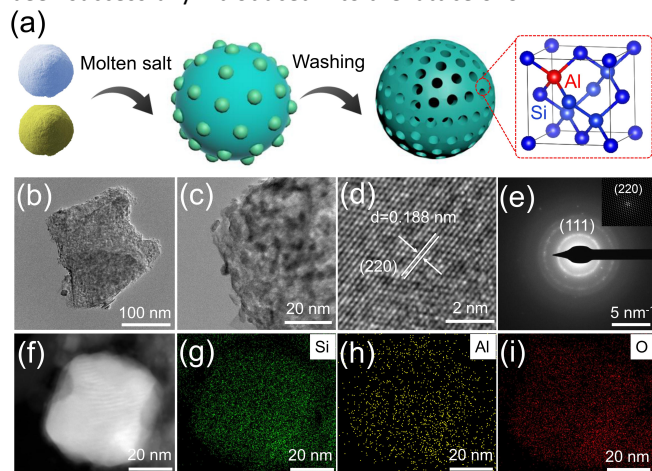


**Fig. 1** (a) Synthesis illustration and crystal structure of pSi-Al. (b,c) TEM images of SA300. (d) HRTEM image of SA300. (e) SAED pattern and lattice puncta after FFT of SA300. (f) HAADF image of SA300. (g~i) Elemental mapping images Si; Al; O.

The XRD of SA300 was shown in Fig 2(a). All of the peaks can be index to Si standard card (JCPDS 27-1402). Then, the obtained unit cell parameter were: a= 5.43024 Å, Vol= 160.124 Å$^3$, density= 2.33 g cm$^{-2}$. Comparing with the standard card (JCPDS 27-1402, where, a= 5.43088 Å, Vol= 160.2 Å$^3$, density= 2.329 g cm$^{-2}$), SA300 had decreased lattice constant and volume. Meanwhile, XRD of pSi-Al were shown in Fig. S3(a) from 250 to 450 ℃. The localized magnification of peak (111) showed the position shifted to the right and then to the left as the temperature increased. The maximum shift was at 300 ℃ (Fig. S3(b)). Raman spectra showed the main vibration peaks. It derived from Si-Si bonds and the maximum deviation was at 300 ℃ (Fig. 2(b) and (c)), which meant the highest doping content. The X-ray photoelectron spectroscopy (XPS) survey scan demonstrated SA300 consisted of Si, Al, and O (Fig. 2(d)). The Al high-resolution spectra peak located at 73.84 eV was obviously observed (Fig. 2(e)). The peaks of Si located at 103.59 eV, 102.9 eV, 99.76 eV and 99.23 eV could be attributed to Si$^{2+}$, Si$^{1+}$, and Si 2p, respectively (Fig. 2(f)). The accurate content of Al was confirmed by inductively coupled plasma mass spectrometry (ICP-MS) (Fig. 2(g)) and the maximum content was 4.46 % for SA300. Furthermore, the content gradually decreased with temperatures over 300 ℃, which agreed with the XRD and Raman results. The peak positions of the SA250 and SA300 in the Li spectrum were different (Fig. S7(b) and (e)). It was due to the interaction between Al$^{3+}$ and Li$^+$ after Al doping. The peak position of SA300 was located at 55.35 eV, and that of SA250 was located at 55.08 eV, which had the 0.27 eV shift. It was found that the proportion of LiF in SA300 was higher than SA250 after fitting. Therefore, Al doping could directly affect the formation of SEI components, which was more favorable to the formation of LiF. It could effectively protect the SEI structure in cycling.

Fig. 2(h) displayed N$_2$ adsorption and desorption isotherm and pore diameter distribution. Specific surface area of 162 m$^2$ g$^{-1}$ and average pore diameter of 4.03 nm were presented for SA300. Meanwhile, specific surface areas of 217 m$^2$ g$^{-1}$, 72 m$^2$ g$^{-1}$, 45 m$^2$ g$^{-1}$ and 44 m$^2$ g$^{-1}$ were recorded for SA250, SA350, SA400, and SA450, respectively (Fig. 2(i)). However, the pore diameter showed opposite tendency.
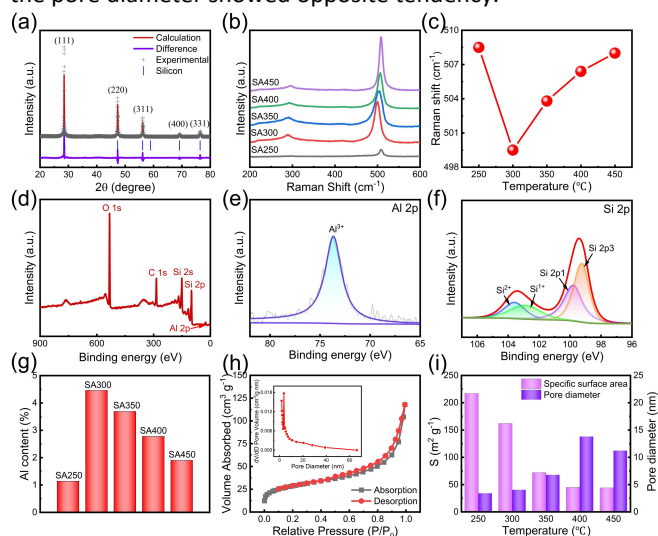


**Fig. 2** (a) XRD pattern of SA300. (b) Raman patterns of pSi-Al. (c) Plot of Raman peak changes. (d) XPS survey of SA300. (e,f) Al 2p and Si 2p high-resolution XPS spectra. (g) ICP results of Al content. (h) N$_2$ adsorption and desorption isotherm and pore diameter distribution curves. (i) Specific surface area and pore diameter statistics.

We have found that the SA300 showed the ICE of 90.57 %, while the SA250 was 70 % (Fig. 3(a) and (b)). Considering similar porous structures, the significant differences of ICE derived from Al doping content. It is known that the effect of Li capture in silicon anodes is responsible for around 30 % of initial Li loss.[17] Therefore, the key to raising ICE is to reduce Li capture. To find the reason of higher ICE, the mechanism was explored. Firstly, volume expansion was investigated after the first cycle (Fig. S4(a~h)). No apparent crushing was found in both electrodes. The thickness of SA300 was measured ranged from 5.526 um to 5.767 um, while SA250 ranged from 7.048 um to 7.392 um. It meant initial Li loss was hardly due to volume expansion.

To ascertain the effect of SEI, TEM was conducted. The thickness of SEI were 19.17 nm and 19.62 nm for SA300 and SA250, respectively (Fig. S4(i) and (j)). Electrochemical impedance spectroscopy (EIS) was conducted to explore the growth of SEI (Fig. 3(c)). The two high-frequency semicircles and the low-frequency slash suggested the creation of SEI, the charge transfer reaction at the electrode-electrolyte interface, and the Li$^+$ diffusion process, respectively. The fitted R$_{SEI}$ were 60.8 Ω and 65.9 Ω, respectively, which agreed

**COMMUNICATION**

with TEM (Fig. S4(i) and (j)). Therefore, the SEI formation did not exhibit significant differences.

Subsequently, the Li capture was taken into consideration. The Li$^+$ concentrations in the SEI of SA250 and SA300 were measured to be 13.57 mg L$^{-1}$ and 8.136 mg L$^{-1}$, respectively (Fig. 3(d)). Meanwhile, the captured Li$^+$ concentrations were 1.184 mg L$^{-1}$ and 1.004 mg L$^{-1}$. The Li$^+$ capture of SA300 decreased by 15.2 % compared with SA250. The peak positions of the SA250 and SA300 in the Li spectrum were different (Fig. 3(e) and (f)). It was due to the interaction between Al$^{3+}$ and Li$^+$ of SA300 after Al doping. The peak position of SA300 was at 55.35 eV, and that of SA250 was at 55.08 eV, which had the 0.27 eV shift. It was found that the proportion of LiF in SA300 electrode was higher than SA250 after fitting, thus it can effectively protect the SEI structure in cycling. Therefore, Al doping could directly affect the formation of SEI components in cycling, which was more favorable to the formation of LiF. It greatly improved the ICE of porous silicon together with the reduction of lithium capture.
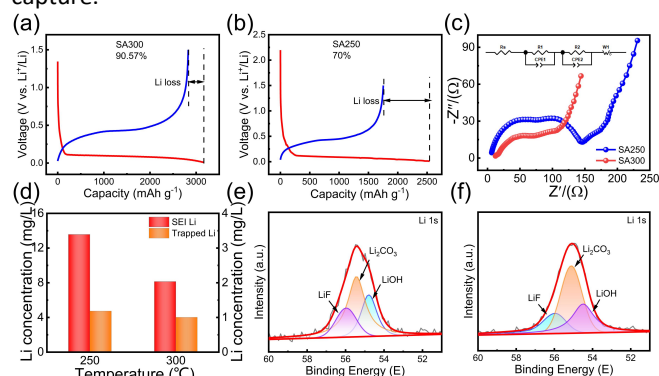


**Fig. 3** Initial charge/discharge voltage profiles. (a) SA300. (b) SA250. (c) EIS of SA300 and SA250 after the first cycle. (d) SEI Li$^+$ and trapped Li$^+$ of SA300 and SA250. (e) Li 1s high-resolution XPS spectra of SA300. (f) Li 1s high-resolution XPS spectra of SA250.

The cyclic voltammetry (CV) was used to explore Li storage performance. It revealed initial three cycles with a scan rate of 0.1 mV s$^{-1}$ and voltage from 0.01 to 1.5 V (Fig. 4(a)). The reduction peak was observed below 0.1 V during the first discharge. It corresponded to the creation of Li$_x$Si alloy, and the hardly distinguishable reduction peak indicated stable SEI formation and minimal capacity loss. Subsequently, a new reduction peak appeared at 0.17 V. Then, the oxidation peaks appeared at 0.35 V and 0.52 V. Additionally, the location of anodic and cathodic peaks remained almost the same. The steady increase in peak currents suggested gradual activation of pSi-Al.[26] No peaks of Li-Al interaction emerged, indicating Al doping mainly enhanced the conductivity.
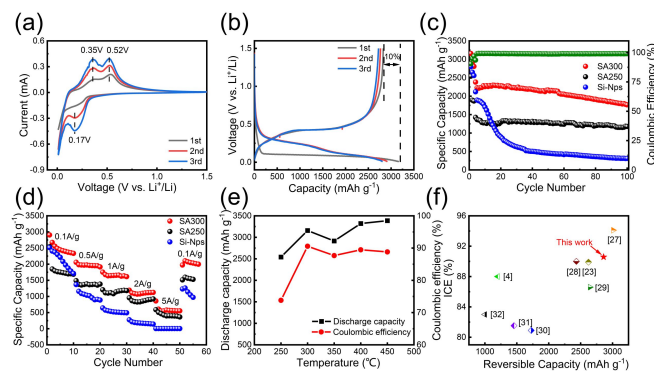


**Fig. 4** (a) CV profiles of SA300 at 0.1 mV s$^{-1}$. (b) Charge/discharge voltage profiles of SA300 at 100 mA g$^{-1}$. (c) Cycle performance at 1.0 A g$^{-1}$. (d) Rate performance. (e) Comparison of pSi-Al materials. (f) Comparison of ICE and reversible capacity in silicon anodes literature.

The corresponding charging/discharging voltage profiles of SA300 at 100 mA g$^{-1}$ were displayed in Fig. 4(b). A clear plateau appeared at 0.1 V during the first discharge. The initial capacity loss primarily occurred during the SEI formation that accompanied with irreversible Li$^+$ capture and vanished in the subsequent processes. The Coulombic efficiency increased to 95 % and 97 % in the second and third cycle. The ensuing profiles nearly overlapped, indicating excellent reversibility.

The cycle performance of Si-Nps, SA300 and SA250 at 1.0 A g$^{-1}$ were investigated (Fig. 4(c)), which showed reversible capacities of 1894 mAh g$^{-1}$, 2382 mAh g$^{-1}$, and 1424 mAh g$^{-1}$, respectively. In the fifth cycle, the SA300 achieved a coulombic efficiency over 99 %. Moreover, it remained reversible capacity of 1765 mAh g$^{-1}$ after 100 cycles. It should be noted that the outstanding cycling stability of pSi-Al without any carbon coatings. At the same time, the Si-Nps underwent rapid decay in capacity after 20 cycles. Fig. S5 compared cycle performances at each temperature. Apparently, SA300 had improved cycling stability. The long-term cycle performance of SA300 was shown in Fig. S6. The reversible capacity remained at 835.4 mAh g$^{-1}$ after 300 cycles at 1 A g$^{-1}$.

The rate performance of Si-Nps, SA300 and SA250 were also studied (Fig. 4(d)). The reversible capacities of SA300 from 0.1 A g$^{-1}$ to 5 A g$^{-1}$ were 2905 mAh g$^{-1}$, 2058 mAh g$^{-1}$, 1754 mAh g$^{-1}$, 1193 mAh g$^{-1}$ and 607 mAh g$^{-1}$, respectively. The SA250 exhibited 2544 mAh g$^{-1}$, 1489 mAh g$^{-1}$, 1206 mAh g$^{-1}$, 957 mAh g$^{-1}$, and 588 mAh g$^{-1}$. The Si-Nps exhibited 2513 mAh g$^{-1}$, 1368 mAh g$^{-1}$, 643 mAh g$^{-1}$, 276 mAh g$^{-1}$ and 4.2 mAh g$^{-1}$. The reversible capacities of SA300 and SA250 recovered to 2104 mAh g$^{-1}$ and 1511 mAh g$^{-1}$ when the current density returned to 0.1 A g$^{-1}$. It suggested superior structural stability of pSi-Al. The initial discharge capacity and ICE of pSi-Al were shown in Fig. 4(e) and SA300 had the highest ICE. The ICE and reversible capacity were compared with recent reports (Fig. 4(f)).[4, 23, 27-32]

To assess the Li$^+$ diffusion kinetics, the CV of SA300 and SA250 with scan rates from 0.1 to 1 mV s$^{-1}$ were taken (Fig. 5(a) and (b)), which showed similar redox peaks shape. The

peak current progressively rose as scan rate increased. Potential difference was small between the redox peaks, indicating less electrochemical polarization.[33] The $Li^+$ storage includes two aspects: $Li^+$ diffusion and capacitance, and the relationship between peak current (i) and scan rate (v) could be described with equations (2) and (3).[34]

$$i=av^b \quad (2)$$

$$\log i=\log a+b\log v \quad (3)$$
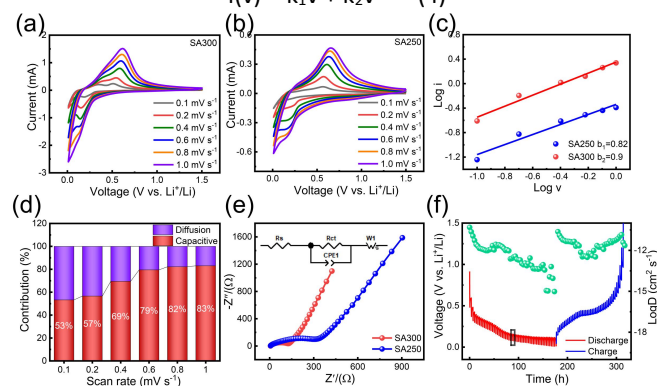
$$i(v) = k_1v + k_2v^{1/2} \quad (4)$$



**Fig. 5** CV profiles at various scan rates (a) SA300. (b) SA250. (c) Linear relationship between log i and log v for SA300 and SA250. (d) Capacitance and diffusion control contribution of SA300. (e) EIS comparison between SA300 and SA250 before cycling. (f) GITT profiles and calculated D of SA300.

The SA300 and SA250 had the fitted b values of 0.9 and 0.82 (Fig. 5(c)), which indicated the co-controlled process. Furthermore, capacity control mechanism can be calculated by the equation (4).[35] Where i(v) is the total current, $k_1v$ and $k_2v^{1/2}$ are the processes of pseudocapacitance and diffusion-controlled contribution.[36] The pseudocapacitance contribution gradually increased as scan rate increased (Fig. 5(d)). It reached 83 % at 1.0 mV $s^{-1}$ (Fig. S9(a)). The EIS of SA300 and SA250 were displayed in Fig. 5(e) and Fig. S9(c). The fitted Rct before cycling were 112.4 Ω and 311.8 Ω. The Rct after 100 cycles were 86.9 Ω and 351.8 Ω. It further confirmed that Al doping significantly improved the conductivity. Moreover, the larger slope of the slash corresponded to faster $Li^+$ diffusion.[37,38] EIS of the 100th and 200th cycles were also tested, and the Rct were 86.9 Ω and 133.4 Ω (Fig. S9(b)). It suggested that SA300 had substantially reduced charge transfer resistance and $Li^+$ diffusion coefficient.[39,40]

Galvanostatic intermittent titration technique (GITT) was taken and $Li^+$ diffusion coefficient D was calculated by the equation (5):

$$D = \frac{4}{\pi\tau}\left(\frac{m_B V_M}{M_B S}\right)^2\left(\frac{\Delta E_S}{\Delta E_\tau}\right)^2 \quad (5)$$

The obtained D of SA300 was $3.32 \times 10^{-13}$ $cm^2$ $s^{-1}$ to $2.33 \times 10^{-11}$ $cm^2$ $s^{-1}$ in the state of charge (Fig. 5(f) and S9(d)). The overpotential of SA300 was lower than SA250 (Fig. S9(e) and (f)).[41,42]

To confirm the structural integrity of electrodes, the surface morphology was characterized using SEM. The SEM of SA300 before and after 100 cycles were displayed in Fig.

S10(a) and (b). It was observed that the electrode was still intact after cycling although there was minor surface cracking. Moreover, the SEM of SA250 after cycling displayed noticeable alterations in the surface silicon particles, but no appreciable breaking was seen (Fig. S10(c) and (d)).

## Conclusions

In conclusion, we have reported Al-doped porous silicon anode. The improved ICE of 90.57 % was achieved by reducing lithium capture. The maximum Al doping amount could be over 4 % and the $Li^+$ capture had decreased by 15.2 % compared to SA250. Meanwhile, it promoted the formation of LiF in cycling, which demonstrated stabilized SEI. A reasonably designed pSi-Al could effectively buffer volume expansion, which showed accelerated $Li^+$ diffusion kinetics and excellent cycling stability. The electrochemical performance of the pSi-Al was then enhanced by adjusting the reaction temperatures to alter the Al doping amount. The strategy provided a new approach to improve the ICE of silicon-based materials.

## Data availability

The data that support the findings of this study are available from the corresponding author upon reasonable request.

## Conflicts of interest

There are no conflicts to declare.

## Acknowledgements

## References

1.  G. G. Eshetu, H. Zhang, X. Judez, H. Adenusi, M. Armand, S. Passerini and E. Figgemeier, *Nat. Commun.*, 2021, **12**, 5459.

2.  M. Jiang, J. Chen, Y. Zhang, N. Song, W. Jiang and J. Yang, *Adv. Sci.*, 2022, **9**, 2203162.

3.  L. Sun, Y. Liu, R. Shao, J. Wu, R. Jiang and Z. Jin, *Energy Storage Mater.*, 2022, **46**, 482-502.

4.  H. Tian, H. Tian, W. Yang, F. Zhang, W. Yang, Q. Zhang, Y. Wang, J. Liu, S. R. P. Silva, H. Liu and G. Wang, *Adv. Funct. Mater.*, 2021, **31**, 2101796.

5.  X. Min, G. Xu, B. Xie, P. Guan, M. Sun and G. Cui, *Energy Storage Mater.*, 2022, **47**, 297-318.

6.  Z. Cheng, H. Jiang, X. Zhang, F. Cheng, M. Wu and H. Zhang, *Adv. Funct. Mater.*, 2023, **33**, 01109.

7.  Y. Zhang, B. Wu, G. Mu, C. Ma, D. Mu and F. Wu, *J. Energy Chem.*, 2022, **64**, 615-650.

8.  R. Zhan, X. Wang, Z. Chen, Z. W. Seh, L. Wang and Y. Sun, *Adv. Energy Mater.*, 2021, **11**, 2101565.

9.  C. Zu, H. Yu and H. Li, *InfoMat*, 2021, **3**, 648-661.

10. P. Li, J.-Y. Hwang and Y.-K. Sun, *ACS Nano*, 2019, **13**, 2624-2633.

11. G. Zhou, L. Xu, G. Hu, L. Mai and Y. Cui, *Chem. Rev.*, 2019, **119**, 11042-11109.

12. Y.-W. Cheng, C.-H. Chen, S.-A. Wang, Y.-C. Li, B.-L. Peng, J.-H. Huang and C.-P. Liu, *Nano Energy*, 2022, **102**, 107688.

13. K. Wang, S. Pei, Z. He, L.-a. Huang, S. Zhu, J. Guo, H. Shao and J. Wang, *Chem. Eng. J.*, 2019, **356**, 272-281.

14. Y. Tian, Y. An and J. Feng, *ACS Appl. Mater. Interfaces*, 2019, **11**, 10004-10011.

15. Z. Li, Y. Zhang, T. Liu, X. Gao, S. Li, M. Ling, C. Liang, J. Zheng and Z. Lin, *Adv. Energy Mater.*, 2020, **10**, 1903110.

16. W. An, B. Gao, S. Mei, B. Xiang, J. Fu, L. Wang, Q. Zhang, P. K. Chu and K. Huo, *Nat. Commun.*, 2019, **10**, 1447.

17. C.-Z. Ke, F. Liu, Z.-M. Zheng, H.-H. Zhang, M.-T. Cai, M. Li, Q.-Z. Yan, H.-X. Chen and Q.-B. Zhang, *Rare Met.*, 2021, **40**, 1347-1356.

18. L. Lin, Y. Ma, Q. Xie, L. Wang, Q. Zhang and D.-L. Peng, *ACS Nano*, 2017, **11**, 6893-6903.

19. H. Song, H. X. Wang, Z. Lin, X. Jiang, L. Yu, J. Xu, Z. Yu, X. Zhang, Y. Liu, P. He, L. Pan, Y. Shi, H. Zhou and K. Chen, *Adv. Funct. Mater.*, 2016, **26**, 524-531.

20. J. Lu, D. Li, L. Li, Y. Chai, M. Li, S. Yang and J. Liang, *J. Mater. Chem. A*, 2018, **6**, 5926-5934.

21. J. Zhou, H. Zhao, N. Lin, T. Li, Y. Li, S. Jiang, J. Tian and Y. Qian, *J. Mater. Chem. A*, 2020, **8**, 6597-6606.

22. Z. Xu, Y. Hou, J. Guo, J. Wang and S. Zhou, *ACS Appl. Energy Mater.*, 2021, **4**, 14141-14154.

23. Q. Ma, Y. Zhao, Y. Guo, Z. Zhao, H. Xie, P. Xing, D. Wang and H. Yin, J. Mater. Chem. A, 2022, 10, 10004-10013.

24. J. Han, S. Jo, I. Na, S.-M. Oh, Y.-M. Jeon, J.-G. Park, B. Koo, H. Hyun, S. Seo, D. Lee, H. Kim, J. Kim, J.-C. Lim and J. Lim, *ACS Appl. Mater. Interfaces*, 2021, **13**, 52202-52214.

25. J. Zhang, S. Li, F. Xi, X. Wan, Z. Ding, Z. Chen, W. Ma and R. Deng, *Chem. Eng. J.*, 2022, **447**, 137563.

26. D. Rehnlund, F. Lindgren, S. Bohme, T. Nordh, Y. Zou, J. Pettersson, U. Bexell, M. Boman, K. Edstrom and L. Nyholm, *Energy Environ. Sci.*, 2017, **10**, 1350-1357.

27. B. Zhu, G. Liu, G. Lv, Y. Mu, Y. Zhao, Y. Wang, X. Li, P. Yao, Y. Deng, Y. Cui and J. Zhu, *Sci. Adv.*, 2019, **5**, eaax0651.

28. G. Hou, B. Cheng, Y. Yang, Y. Du, Y. Zhang, B. Li, J. He, Y. Zhou, D. Yi, N. Zhao, Y. Bando, D. Golberg, J. Yao, X. Wang and F. Yuan, *ACS Nano*, 2019, **13**, 10179-10190.

29. X. Zhang, D. Wang, X. Qiu, Y. Ma, D. Kong, K. Muellen, X. Li and L. Zhi, *Nat. Commun.*, 2020, **11**, 3826.

30. J. Shi, L. Zu, H. Gao, G. Hu and Q. Zhang, *Adv. Funct. Mater.*, 2020, **30**, 2002980.

31. Z. He, Z. Xiao, H. Yue, Y. Jiang, M. Zhao, Y. Zhu, C. Yu, Z. Zhu, F. Lu, H. Jiang, C. Zhang and F. Wei, *Adv. Funct. Mater.*, 2023, **33**, 00094.

32. C. Xu, L. Shen, W. Zhang, Y. Huang, Z. Sun, G. Zhao, Y. Lin, Q. Zhang, Z. Huang and J. Li, *Energy Storage Mater.*, 2023, **56**, 319-330.

33. D. Dai, X. Zhou, P. Yan, Z. Zhang, L. Wang, Y. Qiao, C. Wu, H. Li, W. Li, M. Jia, B. Li and D.-H. Liu, ACS Appl. Mater. Interfaces, 2024, 16, 2428-2437.

34. J.-L. Yang, X.-X. Zhao, W. Zhang, K. Ren, X.-X. Luo, J.-M. Cao, S.-H. Zheng, W.-L. Li and X.-L. Wu, ANGEW CHEM INT EDIT, 2023, 62, 2300258.

35. R. Yu, Y. Pan, Y. Liu, L. Zhou, D. Zhao, J. Wu and L. Mai, ACS Nano, 2023, DOI: 10.1021/acsnano.2c10381, 2c10381.

36. J. Fei, S. Zhao, X. Bo, F. Xie, G. Li, E.-A. M. A. Ahmed, Q. Zhang, H. Jin and Z. Lin, Carbon Energy, 2023, 5, 333.

37. J. Sun, B. Li, C. Jin, L. Peng, D. Dai, J. Hu, C. Yang, C. Lu and R. Yang, J. Power Sources, 2021, 484, 229253.

38. K.-Y. Zhang, Y.-Q. Fu, H.-H. Liu, J.-L. Yang, M.-Y. Su, Y. Wang and X.-L. Wu, Phys. Scr., 2023, 98, 125977.

39. Y.-F. Meng, H.-J. Liang, C.-D. Zhao, W.-H. Li, Z.-Y. Gu, M.-X. Yu, B. Zhao, X.-K. Hou and X.-L. Wu, J. Energy Chem., 2022, 64, 166-171.

40. W. Huang, S. Liu, R. Yu, L. Zhou, Z. Liu and L. Mai, Energy Environ. Mater., 2023, 6, 12466.

41. S. Zhao, Y. He, Z. Wang, X. Bo, S. Hao, Y. Yuan, H. Jin, S. Wang and Z. Lin, Adv. Energy Mater., 2022, 12, 2201015.

42. S. Zhao, C. D. Sewell, R. Liu, S. Jia, Z. Wang, Y. He, K. Yuan, H. Jin, S. Wang, X. Liu and Z. Lin, Adv. Energy Mater., 2020, 10, 1902657.

1
2
3
4
5
6
7
8
9
10
11
12
13
14
15
16
17
18
19
20
21
22
23
24
25
26
27
28
29
30
31
32
33
34
35
36
37
38
39
40
41
42
43
44
45
46
47
48
49
50
51
52
53
54
55
56
57
58
59
60

**Data availability**

The data that support the findings of this study are available from

the corresponding author upon reasonable request.